Journal of Power Sources 334 (2016) 128–136

Contents lists available at ScienceDirect

Journal of Power Sources

journal homepage: www.elsevier.com/locate/jpowsour

Semimicro-size agglomerate structured silicon-carbon composite as an anode material for high performance lithium-ion batteries

Hiesang Sohn [a], Dong Hyeon Kim [b], Ran Yi [a], Duihai Tang [a], Sang-Eui Lee [c], Yoon Seok Jung [b, **], Donghai Wang [a, *]

[a] The Pennsylvania State University, Department of Mechanical and Nuclear Engineering, University Park, PA, 16802, USA
[b] Ulsan National Institute of Science and Technology (UNIST), School of Energy and Chemical Engineering, Department of Energy Engineering, Ulsan, 689-798, South Korea
[c] University of California, Los Angeles (UCLA), Mechanical and Aerospace Engineering Department, Los Angeles, CA, 90095, USA

HIGHLIGHTS

- *m*Si-C: Semimicro-size Si-carbon composite as an anode material for Li-ion battery.
- Facile preparation through an aerosol-assisted process and carbon coating.
- Agglomerate structured Si NPs with conformally formed carbon layer.
- Good cycle stability: 96% capacity retention (1999 mAh/g) after 50 cycles.
- Good rate capability: high capacity (906 mAh/g) at high current density (12 A/g).

ARTICLE INFO

Article history:
Received 1 June 2016
Received in revised form
18 August 2016
Accepted 17 September 2016
Available online 12 October 2016

Keywords:
Semimicro-size silicon-carbon composite
Agglomerate structure
Aerosol process
Lithium-ion battery anode

ABSTRACT

A semimicro-size agglomerate structured silicon-carbon (*m*Si-C) composite is constructed by an aggregation of silicon nanoparticles (~100 nm) coated with conductive carbon layer through a facile and scalable aerosol-assisted process to be employed as an anode material for lithium-ion batteries (LIBs). As-formed *m*Si-C composite delivers good electrochemical performances of high reversible capacity (2084 mAh/g) between 0.01 and 1.50 V (*vs.* Li/Li^+) at 0.4 A/g, 96% capacity retention (1999 mAh/g) after 50 cycles and good rate capability (906 mAh/g) at 12 A/g. Such good performances can be attributed to 1) unique composite structure which accommodates the stress induced by volume change of silicon during lithiation/delithiation and facilitates ion transport, and 2) conformally formed carbon layer which enhances conductivity of the composite and helps to form a stable SEI layer. In addition, a high tap density (0.448 g/cm^3) of *m*Si-C composite leads to high volumetric capacity (933 mAh/cm^3), allowing its practical applications as an anode material towards high performance LIBs.

1. Introduction

As of recent introduction of electric vehicles (EV) into automobile market, continuous and massive demands for lithium-ion batteries (LIBs) with high energy/power densities and long life cycle have triggered to develop inexpensive, high energy/power density electrode materials [1–6]. Thus far, graphite based anodes have been used in commercial LIBs but its low theoretical capacity (~372 mAh/g) limits the mileage of EV per charge [1–6]. Hence, it is essential to develop novel LIB anode materials for next generation EV with high energy/power densities and long duration time at economical cost [1–6].

In this context, silicon (Si) has been extensively studied as a suitable anode material for high energy density LIBs owing to its high specific capacity (~3580 mAh/g) and natural abundance [2–5]. However, practical application of Si based anodes is still hindered due to their unsatisfactory performance (fast capacity fading and poor rate performance) mainly caused by huge volumetric change of Si (>400%) during lithiation/delithiation; such a huge change of Si causes several problems including unstable solid electrolyte interphase (SEI) formation, disintegration of electrode structure

* Corresponding author.
** Corresponding author.
E-mail addresses: ysjung@unist.ac.kr (Y.S. Jung), dwang@psu.edu (D. Wang).

http://dx.doi.org/10.1016/j.jpowsour.2016.09.096
0378-7753/

and poor electrical contact among electrode materials [6].

Accordingly, many studies have been devoted to addressing aforementioned issues mainly through 1) reducing the size of Si particle [2,3,7–10], 2) making the composite of Si and carbonaceous agent [7,8,10–20] and 3) formation of the metal oxide layer on Si [20]. First, smaller sized Si based anodes have been demonstrated by constructing various nanostructured silicon (e.g., Si nanospheres [7,8], Si nanowires [2], Si nanotubes [3] and nanoscale ultrathin Si films [9,10]). For instance, based on the work of Liu et al. who theoretically revealed the crucial role of small-sized Si (<150 nm) electrode to sustain the structure of Si particles without cracked nor fractured by first lithiation-induced swelling [11], Kim et al. and many other researchers reported superior performance (specific capacity > *ca.*1000 mAh/g over 50 cycles) of nano-sized Si electrodes to bulk Si electrodes [2–11]. As demonstrated by previous reports, the improved performance of nano-sized Si electrodes is attributable to effective accommodation of large stress or applied strain by small sized Si upon lithiation, which alleviates pulverization of electrode materials as well as keeps electrical contact of Si particles. Additionally, small sized Si enables the short ionic transport distance of lithium ions, allowing their facile mass transport during the process [5]. Second, compositing Si with carbonaceous agent such as carbon, CNT and graphene results in improved electrochemical performance [7,8,10–19]. For instance, there have been many reports on construction of silicon nanocomposites based electrodes (e.g., Si-C [7,8,11–17], Si-graphene [18] and Si-CNT [19]) which exhibit enhanced LIBs performance (long capacity retention and high rate capability). Ng et al. reported around 1857 mAh/g at 0.15 A/g using Si@C nanocomposite [7]. Jung et al. demonstrated high performance anode (1469 mAh/g after 50 cycles at 1 A/g) using nanostructured Si@porous carbon composite [8]. Zhou et al. presented Si/graphene nanocomposite which exhibits much superior cycle performance (1153 mAh/g at 0.2 A/g after 100 cycles) and rate capability (803 mAh/g at 4 A/g) to that of pristine Si nanoparticles (<10 mAh/g at 0.2 A/g after 50 cycles) [18]. Gohier et al. demonstrated Si decorated CNT which shows good cycle performance (57% capacity retention at 35.8 A/g after 100 cycles) and excellent rate capability (760 mAh/g at 53.7 A/g) [19]. Improved performance of Si-carbonaceous agent composite electrodes can be attributed to the role of conductive agents that electronically bridge/connect the Si, making the composite more conductive and thus facilitating electron transport in the electrodes [17–19]. Third, protective coating of thin metal oxide layer (e.g., SiO_x and TiO_2) on the Si nanoparticle leaded to an improved electrochemical performance because of formation of stable SEI layer [20]. There are also many reports on composite of Si and metal oxides (e.g., Si-SiO_x, Si-TiO_2 and Si-SiO_2-C) to improve the electrochemical performance [20]. McCormac et al. reported porous Si-TiO_2 nanofiber composite which delivered high reversible capacity (839 mAh/g) and 50% capacity retention after 180 cycles at 0.135 A/g [20]. Liu et al. reported Si-Si oxycarbide (Si-O-C) nanocomposite exhibiting high reversible capacity (1190 mAh/g) and 76% of capacity retention within 20 cycles [20]. Park et al. reported Si-embedded SiO_x nanocomposite with a high capacity (1914 mAh/g) and improved cycle stability over 100 cycles (capacity >1500 mAh/g) at 0.2 A/g [20]. The improved performance of metal-oxide-Si composite can be attributed to the function of metal oxide as a mechanical buffer layer against the severe volume change of Si [20].

However, there are still several technical barriers which hamper practical application of Si materials [14,21]. First, low tap density of Si nanoparticles (Si NPs) leads to far lower volumetric energy density compared with commercial graphite [14,21]. Second, Si NPs can generate several health and safety issues including inhalation and explosion risks during dealing with them in the work place [22]. Although it is logical to develop bigger-sized (micro-sized) Si materials to enhance volumetric energy density [14,21,23], current micro-sized Si electrode suffer from many obvious disadvantages including 1) more liable to pulverization by volume change of Si during lithiation/delithiation and 2) long ion/electron transport paths, which result in capacity fading and poor rate capability [14,21]. Thus, pros and cons of conventional Si materials above have required the development of secondary agglomerate of micro-size Si superstructure built on nano-sized particles as primary building blocks to utilize advantages of both micro-sized and nano-sized Si materials [14,17,21].

There have been several reports on the secondary agglomerate structure of micro-sized Si materials constructed with nanoscale building blocks which show impressive performances [12–14,17,21,23]. Construction of agglomerate structured micro-sized Si was demonstrated mainly through aggregation of nanoparticles, compositing Si with preformed conductive carbon by chemical vapor deposition (CVD) process and thermal disproportionation of Si precursors [12–14,17,21,23]. For instance, Cho and Park et al. produced agglomerate structured micro-sized porous Si-C composites by catalytic etching of micro-sized Si followed by conductive carbon coating, which showed stable capacity retention within 70 cycles [12]. Yushin et al. reported a agglomerate structured micro-sized porous carbon-silicon composite with a high tap density (0.49 g/cm^3) by Si deposition onto porous carbon via a chemical vapor deposition (CVD) process, which exhibited a high volumetric capacity (1270 mAh/cm^3) at a high current density (149 mA/g) and good capacity retention within 100 cycles [17]. Wang et al. and Park et al. reported agglomerate structured micro-sized porous Si-C composites through thermal disproportionation of SiO followed by conductive carbon coating using acetylene gas as a carbon source, exhibiting good electrochemical performance (1459 mAh/g at 1 A/g after 200 cycles) [14,21]. Recently, Liu et al. prepared pomegranate structured micro-sized Si through aggregation and polymerized encapsulation of Si NPs using Si NP, resorcinol and CNT as conductive percolating matrix for active material, showing excellent cycling stability (1160 mAh/g after 1000 cycles at 2.1 A/g) and high coulombic efficiency (99.87%) [23]. Nonetheless, to date, synthesis of such superstructured micro-size Si and its composite materials still remains as a challenge because rather complicated current synthetic processes are not adequate for commercial scale as well as require expensive chemical/physical facility using toxic precursors (e.g., SiH_4) [2–5,10–15,18–21,23].

Aware of these backgrounds, herein, we report a semimicro-size agglomerate structured Si-C (*m*Si-C) composite by interconnection of Si NPs covered with carbon layer. The synthetic process for semimicro-size composite of carbon coated Si NPs involves 1) an aerosol process to form a agglomerate structure of Si NPs and polymer (polyacrylic acid) through evaporation induced assembly and 2) conductive carbon layer deposition as inspired by our previous work [14,24]. Different from previously reported agglomerate structured Si-C composites by complicated syntheses, our synthesis and *m*Si-C composite have several advantageous features of 1) facile and scalable fabrication of composites by commercially available aerosol process, 2) tunable precursor composition (e.g., Si NP or carbon source), 3) formation of aggregated aerosol product constructed from homogeneously mixed precursor, and 4) well-defined agglomerate superstructure at the secondary particle level. The as-formed *m*Si-C composite shows excellent capacity retention of 96% after 50 cycles (1999 mAh/g) due to unique structure of *m*Si-C composite; where the interparticle space in the composite can accommodate the volume expansion of Si and the homogeneously formed carbon layer ensures electrical conduction pathways. We believe that such advantages of our *m*Si-C composite (excellent performance, economical cost and facile/scalable

synthetic process) make our composite a promising anode material candidate for high performance LIBs.

2. Experimental

2.1. Synthesis of the semimicro-size agglomerate structured silicon-carbon composites

2.1.1. Semimicro-size Si-PAA composite (mSi-PAA)

Commercially available silicon nanoparticle (Si NPs: ~100 nm, 98%, Alfa Aesar) were used without further purification. Agglomerate structured silicon-carbon composite particles were synthesized by an aerosol-assisted process, using a precursor of Si NPs and polyacrylic acid (PAA) mixture dispersed in dimethylformamide (DMF). The precursor solution of Si NPs and PAA was supplied into a pneumatic atomizer (model 3076, TSI Inc.) to generate aerosols using nitrogen as a carrier gas (Scheme S1) [24]. The aerosolized precursor passed through a ceramic tube at 400 °C, while solvent evaporation-induced assembly occurs in the aerosol droplet to convert precursor to composited structure of Si NP and PAA. As-formed composited particles (*m*Si-PAA) were collected on membrane filters to be used for subsequent process.

2.1.2. Semimicro-size Si-C agglomerate structured composite (mSi-C)

As-formed *m*Si-PAA composite was placed in a ceramic crucible transferred to be heated to a high temperature tube furnace. The *m*Si-PAA composite particles were coated with a carbon layer through thermal decomposition of acetylene gas at 600 °C for 20 min. For the carbon coating, the gas mixture of acetylene and high-purity argon (argon: acetylene = 9:1 by volume) was supplied into furnace at a flow rate of 100 sccm. Then, calcination was further carried out at 600 °C under argon atmosphere for two hours after carbon coating. The final content of carbon in the *m*Si-C composite was calculated as *ca.* 14 wt% by thermogravimetric analysis (TGA) as shown in Fig. S1.

2.2. Material characterization

The size and morphology of synthesized products were obtained using electronic microscopes of transmission electron microscopy (TEM) and scanning electron microscopy (SEM). TEM images were taken on JEOL-1200 at an accelerating voltage of 80 kV. High-resolution transmission electron microscopy (HR-TEM) images were taken on a field emission microscope (JEOL-2010F) at an accelerating voltage of 200 kV. SEM and energy-dispersive X-ray spectroscopy (EDS) were conducted with a scanning electron microscope (NOVA NanoSEM 630) at accelerating voltages of 1.5 kV and 5 kV. The crystalline structures of material were analyzed by X-ray diffraction (XRD) over a two theta range (10–80°) using a X-ray diffractometer (Rigaku Dmax-2000) with CuKα radiation (λ = 1.5418 Å) under operation voltage and current of 40 kV and 30 mA, respectively. For the pore structure analysis, N_2 sorption isotherms were carried out at 77 K with a porosity analyzer (MicromeriticsASAP2020). Specific surface areas were calculated by Brunauer-Emmett-Teller (BET) method using the adsorption branch of N_2 isotherm in a range of (P/P_o: 0.04–0.25). The pore size distribution was calculated from desorption branch of N_2 sorption curve with Barrett-Joyner-Halenda (BJH) method. The microporosity (micropore surface area) was analyzed by t-plot method. Thermogravimetric analysis (TGA) was carried out using a thermogravimetric analyzer (TA instruments) with a heating rate of 10 °C/min from 25 °C to 900 °C under air atmosphere for the TG-MS analysis. X-ray photoelectron spectroscopy (XPS) was conducted with a Kratos Analytical Axis Ultra XPS. Raman spectroscopy was measured with a confocal Raman instrument (WITec CMR200). Tap density was determined by calculating the ratio of sample mass to its tapped volume [25]. First, a mass of sample in a vial was measured, followed by tapping for 100 times. Then, the tapped volume of sample was measured by reading the thickness of sample in the vial. In the end, the tap densities of samples were finally obtained by calculating the ratio of mass to tapped volume of samples.

2.3. Electrochemical measurements

The working electrodes were prepared by slurry casting on current collector (Cu foil), where the slurry contains active material (*m*Si-C), conductive agent (Super P), and poly(acrylic acid) (PAA) binder (60:20:20 wt ratio) dissolved in 1-methyl-2-pyrrolidinone (NMP, Aldrich). The coated electrodes were dried at 100 °C under vacuum overnight to remove moisture or weakly bound organic moiety. 1.13 cm^2 sized discs were cut from coated electrode to be used as negative electrode (anode). The mass loading of active materials and its electrode thickness is ~1.0 mg/cm^2 and *ca.* 20 μm, respectively. Electrochemical tests were performed with coin cells assembled in an argon-filled glove box (MBraun, Inc.) where lithium foil (99.9%, Aldrich) was used as the counter and reference electrode. A polypropylene porous membrane (Celgard 2400) was used as a separator. A mixture of ethylene carbonate (EC), diethyl carbonate (DEC) and dimethyl carbonate (DMC) (EC: DEC: DMC, 2:1:2 by vol. ratio) with 10 wt% fluoroethylene carbonate (FEC) was used as the electrolyte (Novolyte Technologies). The electrochemical performance was evaluated by galvanostatic charge/discharge cycling on a battery tester (Arbin BT-2000) under various current densities (0.4–12 A/g) in the potential range of 0.01–1.50 V *vs.* Li/Li^+. The current density and specific capacity were calculated based on the mass of active material (*m*Si-C composite). That is, the mass of capacity was normalized to the entire mass of *m*Si-C composite. In the rate capability test, charging rate (lithiation) was fixed at 0.4 A/g during discharge process. AC impedance spectroscopy was performed over a frequency range of 1 MHz-0.01 Hz using a CHI660d electrochemical test station and Solartron electrochemical test station. All electrochemical tests were carried out at room temperature.

3. Results and discussion

Semimicro-size Si-C agglomerate structured composite (*m*Si-C) was synthesized by a two-step process including an aerosol process and subsequent carbon layer deposition at 600 °C, as illustrated in Scheme 1 (and Scheme S1). Typically, ~2 g of *m*Si-C composite was produced per batch. This process is scalable by connecting aerosol apparatuses in parallel. Scheme 1 summarizes the overall synthetic procedure, illustrating the morphological change in the structure of the composite from the precursor to final product. Scheme S1 presents the aerosol setup composed of atomizer connected to a tube furnace and a particle collector.

Briefly, aerosol droplets with sizes of 10–20 μm are continuously generated from a precursor solution containing a mixture solution of Si NPs (~100 nm) and polymer (polyacrylic acid: PAA) dispersed in dimethylformamide (DMF) through an atomization process using nitrogen as carrier gas (Scheme 1a). Note that, PAA was judiciously selected as polymer linker for Si NPs since PAA offer a significantly higher concentration of functional groups and provide with better mechanical properties than conventional cellulose based polymers (e.g., CMC) do [26]. Different from conventional porous structure synthesis using silica as sacrificial template, PAA plays an important role in generating void space as well as in inducing carbon linkage among Si NPs, allowing formation of a

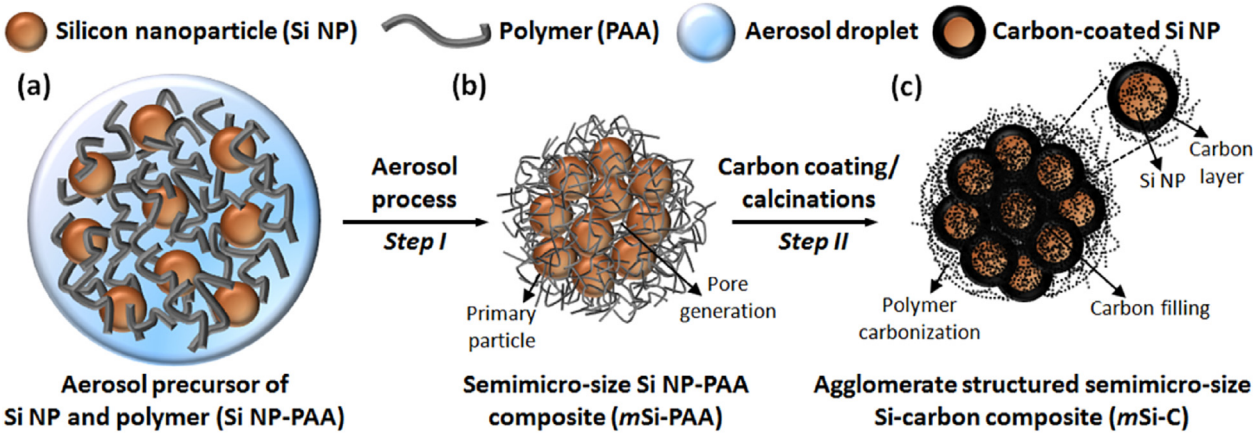

Scheme 1. Formation process of agglomerate structured semimicro-size silicon-carbon (*m*Si-C) composite. (a) Precursor solution of silicon nanoparticles and polymer (PAA) for aerosol process. (b) Superstructured composite of silicon nanoparticle and PAA (*m*Si-PAA) constructed by aerosol process induced agglomeration. (c) Agglomerate structured silicon-carbon composite (*m*Si-C) after carbon coating/calcination.

porous composite structure of uniformly distributed Si NPs connected with PAA. The aerosol droplets pass through a heating zone (400 °C) and are converted into *m*Si-PAA agglomerate superstructured composite; the primary Si NPs are homogeneously mixed with PAA matrix to form three dimensionally integrated Si-PAA composite where pores are generated among the Si NPs interconnected by PAA (Scheme 1b) [24]. Subsequent carbon coating via acetylene carbonization (600 °C, 20 min) and sintering process (600 °C, 2 h) under argon atmosphere convert *m*Si-PAA composite to semimicro-size agglomerate structured Si-C composite (*m*Si-C). Obviously, such a carbon layer deposition and sintering process on the interconnected *m*Si-PAA composite allows carbonization of PAA and carbon filling among the Si NPs thereby enhancing electrical conductivity of the composite (Scheme 1c) [24]. Overall, the synthetic processes (aerosol process and carbon coating process) are easy, controllable and suitable for large-scale synthesis, in contrast to conventional synthetic process requiring harsh conditions (high pressure and temperature), anhydrous and toxic chemicals, and expensive precursors [24].

Fig. 1a shows XRD patterns of as-received silicon (Si), their superstructured intermediate with polymer (*m*Si-PAA) and carbon-coated product (*m*Si-C) obtained at different synthetic stages. The indistinguishable characteristic peaks of silicon for all samples indicate no significant phase change of silicon before and after aerosol process. The average crystalline size of silicon in the final product is estimated as ~20.8 nm by Debye-Scherrer equation. The broad peak appeared around a lower degree (~20°) after carbon coating process is ascribed to amorphous carbon. Fig. 1b displays Raman spectra for *m*Si-PAA and *m*Si-C composite (before and after carbon coating). Three peaks appeared at 297, 513, 517 and 944 cm^{-1} for both *m*Si-PAA and *m*Si-C correspond to characteristic peaks of Si [27]. Small and broad peak around at 297 cm^{-1} are assigned as the 2nd order acoustic phonon mode of Si while strong and sharp peak around 513 or 517 cm^{-1} can be assigned to the 1st order optical phonon mode of crystalline Si [27]. The peak appeared around 944 cm^{-1} is attributed to the formation of native Si-O on the surface of Si nanoparticle [27]. Considering the typical position of bulk Si at 520 cm^{-1}, blue shifted position of Si peak in this work can be attributed to size dependent phonon confinement effect and polycrystalline nature of our Si [27]. What is more, as shown in Fig. 1 and S1, Raman spectra of *m*Si-C shows additional blue shift from 517 cm^{-1} (*m*Si-PAA) to 513 cm^{-1} (*m*Si-C) which originates from the transverse optical mode by a phonon confinement effect, indicating conformal carbon layer deposition on Si nanoparticles [27]. Two characteristic peaks of *m*Si-C at 1321 and 1599 cm^{-1} in the spectra corresponds to D (disordered) and G (graphite) bands of carbon, respectively. Consistent with XRD result (Fig. 2a), the ratio of D to G band is estimated to be 2.3, confirming an amorphous carbon structure [25,27]. The carbon in *m*Si-C composite was estimated to be 14 wt% by thermogravimetric analysis (TGA) result (Fig. S2). Fig. 1c and d shows XPS spectra of Si2p and C1s for *m*Si-PAA and *m*Si-C composite (before and after carbon coating), respectively. For *m*Si-PAA and *m*Si-C, a strong Si2p peak observed around at 99 eV (98.7 and 99.3 eV) corresponds to the binding energy of metallic Si (Si^{0+}SiH) while a small bump centered at around 103 eV suggests the presence of native silicon oxide (SiO_x) layers [28,29]. As compared to *m*Si-PAA, the Si2p signal of *m*Si-C shows shifted peak from 98.7 eV to 99.3 eV and an enhanced peak around 103 eV, indicating more SiO_x formation after carbon coating [29]. We believe that oxygen provided from PAA-derived polymer in *m*Si-PAA might contribute to oxidation of silicon [28,29]. The C1s peaks at 284.5 eV indicates the presence of carbon either from polymer (PAA) or coating layer, implying partial carbonization of PAA by aerosol process at 400 °C [29]. The peak at 289.2 eV of C1s of *m*Si-PAA disappears after carbon coating (*m*Si-C), indicating thermal decomposition of carbonyl group from PAA after sintering at 600 °C [29]. The porosity of the *m*Si-C composite was measured by N_2 sorption isotherms (Fig. S3a) and the pore size distributions (Fig. S3b), showing a surface area of 24.2 m^2/g and a pore volume of 0.047 cm^3/g. The *m*Si-C composite exhibited a similar isotherm curve (type IV) with a condensation step within a narrow relative pressure range and type H1 hysteresis loops.

Fig. 2 exhibits the appearance (Fig. 2a) and morphologies by SEM (Fig. 2b and c) and TEM (Fig. 2d–f) for *m*Si-C before and after carbon layer deposition. Fig. 2a displays the digital photo images of samples before (Top: *m*Si-PAA) and after carbon layer deposition (bottom: *m*Si-C). The photo images clearly show color change from brown (*m*Si-PAA) to black (*m*Si-C), indicating successful carbonization of polymer and carbon layer deposition. The SEM images in Fig. 2b and c demonstrate that the agglomerate structured *m*Si-C composites are consisted of Si NP with carbon layer and their size range is approximately 1 μm as indicated by arrows in Fig. 2c. As shown in Fig. 2d, polysized primary Si NPs (50–150 nm) are around 90 nm in average diameter. Note that, as shown in Fig. 2c and d, primary Si NPs are effectively aggregated and connected with carbon layer, forming agglomerate structured *m*Si-C composite. Arrows in Fig. 2d indicates carbonized polymer and filled carbon in *m*Si-C composite. The TEM image (Fig. 2e–f) displays magnified

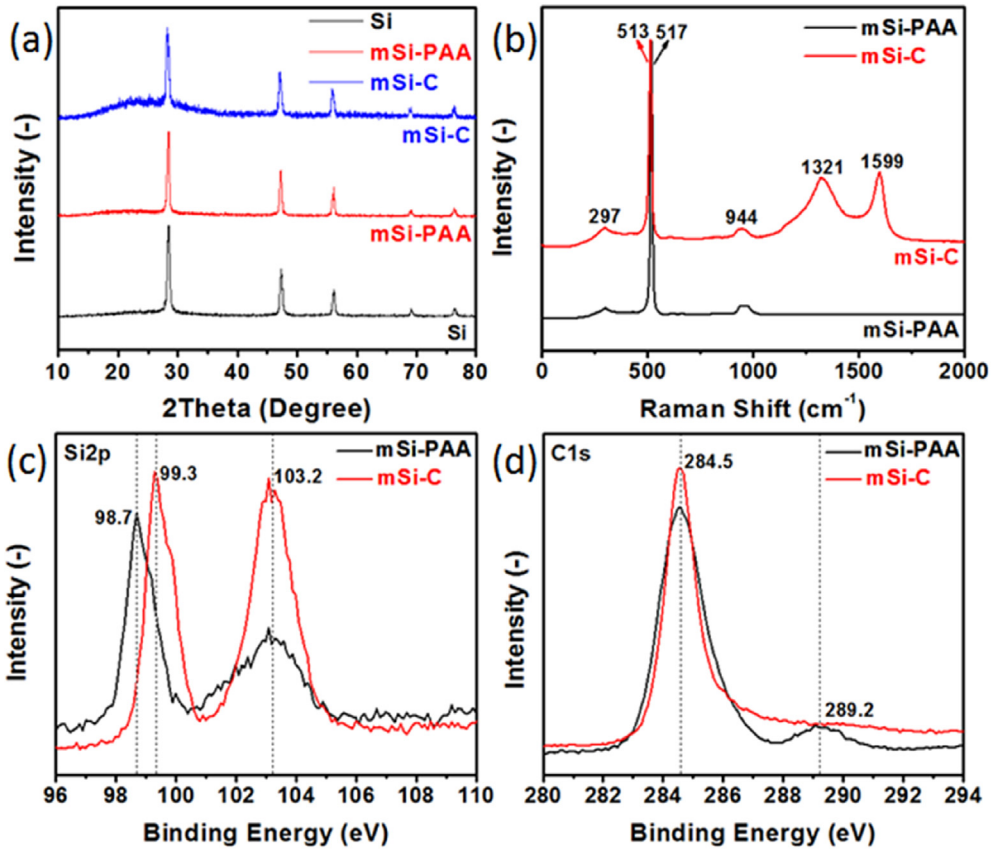

Fig. 1. Structural and surface analysis of *m*Si-C composite obtained at different steps in the synthesis (Si nanoparticle, *m*Si-PAA (after aerosol process), *m*Si-C (after carbon coating) (a) X-ray diffraction patterns; (b) Raman spectra; X-ray photoelectron spectroscopy spectra for (c) Si2p and (d) C1s.

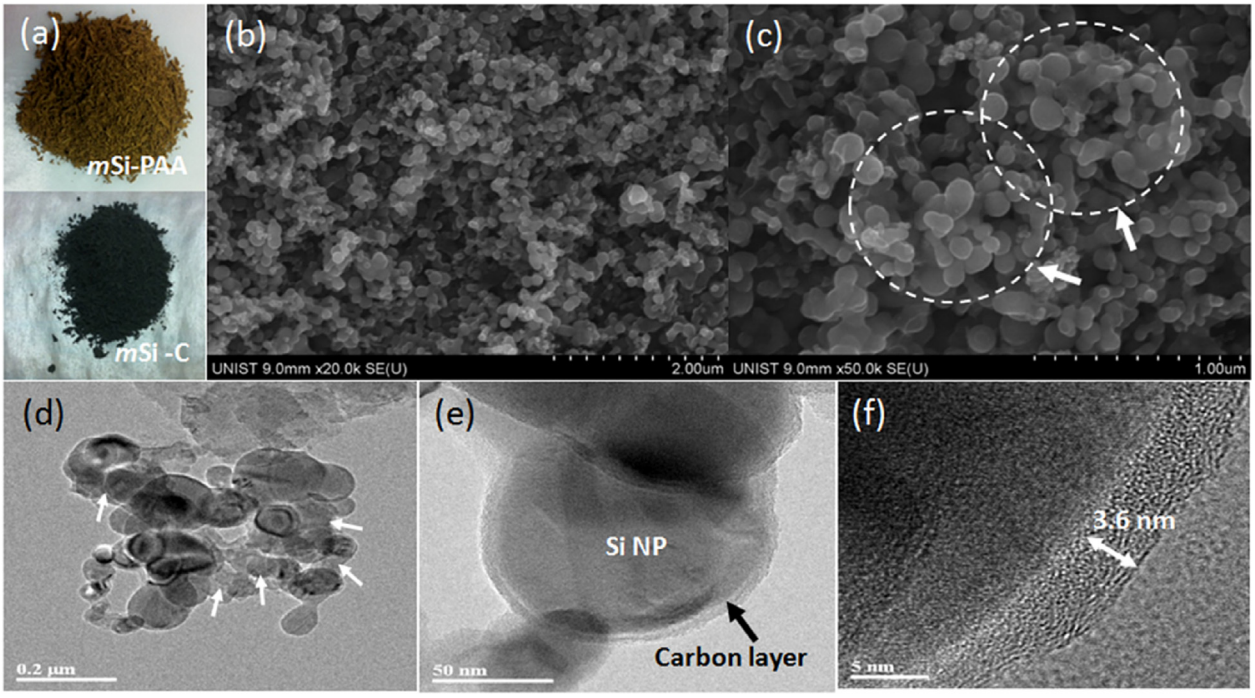

Fig. 2. Visual and electron microscopic characterization of *m*Si-C composite. (a) Photo images of *m*Si-C composite before (top: *m*Si-PAA) and after (bottom: *m*Si-C) carbon coating/calcination; (b–c) SEM images of *m*Si-C composite. Arrows in (c) indicate *m*Si-C composite formed by Si aggregation and carbon layer deposition; (d–e) TEM images of *m*Si-C composite (d) Agglomerate structure of *m*Si-C composite; Arrows in (d) indicate carbonized polymer and filled carbon in *m*Si-C composite formed by carbon coating (e) Magnified image of primiary *m*Si-C composite; (f) high resolution TEM image of *m*Si-C composite.

image of *m*Si-C composite. Fig. 2e demonstrates that primiary particles of *m*Si-C composite are average sized around 90 nm, as consistent with SEM observation (Fig. 2c). The average diameter of aggregated composite is *ca.* 0.7 μm and carbon layers are uniformly deposited on the surface of Si NP. Moreover, these Si NPs are interconnected with each other to form irregular semimicro-size secondary structures of *m*Si-C composite. The high-resolution TEM image (Fig. 2f) further reveals that the thickness of carbon layer of *m*Si-C composite is *ca.* 3.6 nm. A comparable intensity of silicon (red) and carbon (blue) in EDS elemental mapping images (Fig. S4) further indicates homogeneous carbon layer deposition on the surface of Si NPs. As analyzed by TGA (Fig. S1), the silicon and carbon contents of *m*Si-C composite are calculated as 86 and 14 wt %, respectively.

Fig. 3 presents the electrochemical performances of *m*Si-C electrodes. Fig. 3a shows typical voltage profiles of *m*Si-C measured at 0.1C (=0.4 A/g) at the 1st, 2nd, 20th, and 50th cycles. The sloping shapes of voltage profiles are contrasted by well-define plateaus at 0.1 and 0.42 V found in bulk crystalline Si, which reflects the characteristics of nanostructured primary Si [7,21]. Note that, mass of the capacity was normalized to entire mass of *m*Si-C composite. The first discharge (lithiation) and charge (delithiation) capacities are 2535 and 2084 mAh/g, respectively. Considering the Si content (86 wt% from TGA data, Fig. S1), the first charge capacity of *m*Si-C composite implies nearly most of the Si NPs (~82.3%) participate in the charge/discharge process and contribute to such a high gravimetric capacity. The excellent cycling stability and reversibility of *m*Si-C composite are also demonstrated as reflected by almost overlapped voltage profiles of the 20th and 50th cycle. These results suggest that the porous carbon matrix facilitates excellent electronic transports in the composite spheres while buffering the stress caused by severe volume change of the Si core [21,24,28]. Moreover, the first Coulombic efficiency (CE) of *m*Si-C composite was calculated as 82.2%, which is indeed higher than those of other reported Si anode analogues [4,14,21]. Such a high CE can be attributed to unique composite structure of Si core and porous carbon shell, which allows the formation of stable solid electrolyte interphase (SEI) layers during the first cycle [2–5,21,24,28,30,31]. Fig. 3b and Fig. S5 displays the cycling stability and CE of *m*Si-C composite anode at 0.4 A/g. The *m*Si-C shows good capacity retention: 96% (=1999 mAh/g) and 81% (=1694 mAh/g) of the original discharge capacity after 50 and 100 cycles, respectively. In addition to the relatively high initial CE (82.2%), CE at subsequent cycles reaches high values close to 100%. In the cycling range of 1–50, the average CE is 97.9%, and the average CE increases to 98.8% in the cycling range of 51–100. The increased CE can be interpreted as that the SEI layers become stabilized with cycling, and the void space in the conductive carbon matrix of the initial *m*Si-C composite contributes to irreversible SEI formation in the early period of cycling [7,11–15,21]. Note that, the average CE in the later cycles is, still, superior or at least comparable to those of previous studies [12–15,21]. Fig. 3c and d displays cycle stability at a higher current density and rate capability test for the *m*Si-C composite. As shown in Fig. 3c, *m*Si-C has a good capacity retention of 94% (=1469 mAh/g) after 50 cycles and of 80% (1100 mAh/g) after 100 cycles at a higher C-rate of 0.5C (=2 A/g). It is worth to note that there are inconsistent electrochemical behaviors in cycle tests measured at different current densities (Fig. 3b (0.4 A/g) and c (2 A/g)) [32]. At lower current density (0.5 A/g, Fig. 3b), there is no significant capacity decay because of high utilization of Li-ions [33]. In contrast, at higher current density (2 A/g, Fig. 3c), the capacity decay within initial 10 cycles is attributable to insufficient utilization of Li-ions, which may originate from kinetic-driven reactions and decreased electrical contact [33]. After 10 cycles, the capacity gradually

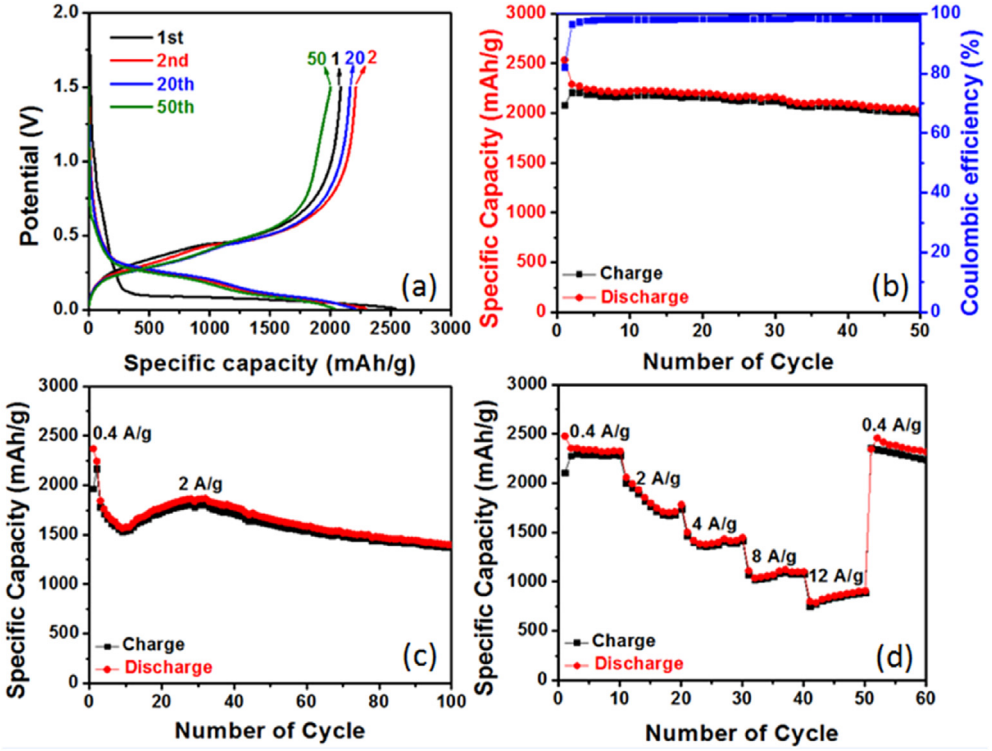

Fig. 3. (a) Galvanostatic charge-discharge voltage profiles, (b) Coulombic efficiency and cycling stability at 0.1C (0.4 A/g), (c) long time cycling stability of *m*Si-C composites at 0.5C (2 A/g), and (d) rate capabilities of *m*Si-C composites from 0.4 to 12 A/g in the potential window 1.5–0.01 V *vs.* Li^+/Li. All the specific capacities are based on the total mass of *m*Si-C composites.

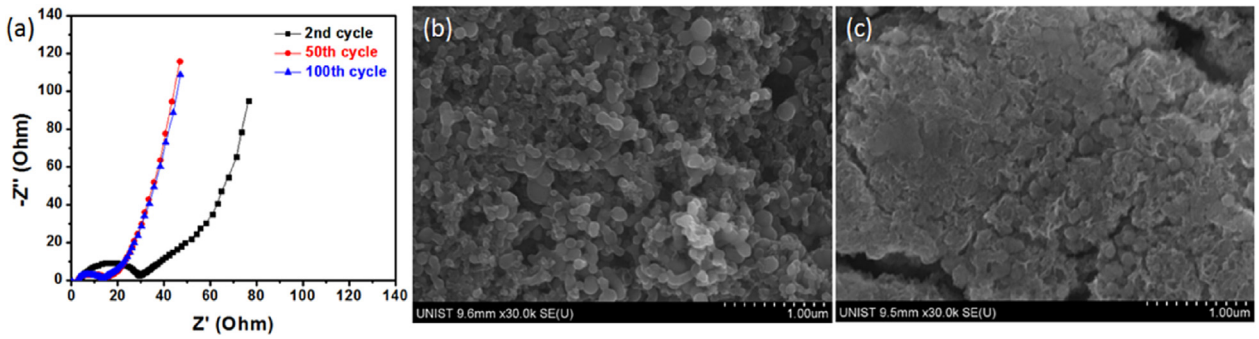

Fig. 4. Nyquist plots of *m*Si-C composite electrode after different numbers of cycles (a), and surface morphology of *m*Si-C electrodes (b) before cycling and (c) after 100 cycles.

recovered and increased, which may be explained by the following activation effects; 1) enhanced wetting of electrodes by electrolyte upon cycling, 2) increased electrode-electrolyte interfacial contact area, caused by repeated dimensional changes of the embedded Si, which might lead to lower the interfacial contact resistance, 3) correspondingly increased contribution by reversible reaction of the SEI layers and/or interfacial charge storage mechanism [34]. In the long-term cycles, however, the slight and gradual decrease of capacity is observed. This can be attributed to uneven stress/strain distribution in Si-C anodes during volume change of Si, induced by local structural inhomogeneous of the electrode structure of Si and carbon, leading to demolished local electronic connections and blocked electrolyte channels [35]. Fig. 3d reveals considerably good rate capability of the *m*Si-C composite. When the current rate was increased 30-fold from 0.1C to 3C, the *m*Si-C composite can still deliver a reversible capacity of 906 mAh/g. Also, when the current rate returned to 0.1C, 94.7% of the original capacity was recovered. Note that, such a good rate capability and cycle stability at high current density can be attributed to unique structure of *m*Si-C composite. The electrochemical performance of *m*Si-C is also compared with that of bare Si and Si-C (super-P) composite containing same elemental content (Si: 86%, C: 14%) (Figs. S6 and S7). Not surprisingly, *m*Si-C shows much superior performance to that of Si-C (Super-P) and bare Si both in cycle test (Fig. S6a and 7a) and in rate-capability test (Fig. S6b and 7b).

Although some of previous works on Si-C nanocomposites shows superior performance, *m*Si-C composite in this work is more advantageous to be commercialized because of its facile and scalable process (production rate: 2 g per batch) without using complicated process or toxic/expensive chemicals. In addition, our excellent rate and cycling performances of *m*Si-C can be mainly attributed to its unique agglomerate structure which keeps and supports electronic/ionic conductivity of the composite during continuous lithiation/delithiation. Detail reasons are summarized as follows [11,14,21,28,30,31].

1. Direct connection of nano-sized Si by aggregation in composite structure facilitates efficient Li diffusion through continuous pores in the composite because of shortened diffusion length of Li-ions, thereby enhancing its ionic conductivity.
2. The small primary Si NPs and void space in the composite could prevent the crumbling of Si cores by alleviation of stress from volume change of Si.
3. Conductive carbon layer connected with the Si can work as a physical buffer and conductive network, which enhances the electrical conductivity of the composite and mitigates the stress from the volume change of Si.
4. Interpenetrating conductive carbon layer can facilitate the formation of a stable SEI layer on the surface of composite and decrease ohmic polarization of the Si in the electrochemical reaction.

As shown in Fig. 4, the excellent cyclability (Fig. 3) of *m*Si-C composites can be better understood by electrochemical impedance spectroscopy (EIS) analysis and comparative observation of morphology for the *m*Si-C composite electrodes before and after cycling at 0.4 A/g. Fig. 4a displays the Nyquist plots of *m*Si-C electrodes after initial, 50, and 100 cycles which consist of two semicircles at high-medium frequency region and a sloped line at low frequency region [11,14,21]. The depressed semicircles are the results of convolution of several contributions: electronic conductivity effects, Li ions transport in the SEI, and the charge transfer resistance at interfaces [2–5,11,14,21]. The sloped line at low frequency is ascribed to the mass transport (diffusion) of Li ions into the Si [11,20]. Comparison of EIS obtained on the cells after initial, 50, and 100 cycles indicates that the *m*Si-C electrode exhibit negligible difference in spectra during these 100 cycles, and also suggests formation of a stable SEI on the *m*Si-C [12,14,21]. The observation of morphological change for *m*Si-C electrode before and after cycling (Fig. 4b and c) also supports the good electrochemical reversibility of the composite as evidenced by EIS results (Fig. 4a). As compared with the SEM image before cycles (Fig. 4b), Fig. 4c reveals that initial morphology of *m*Si-C electrodes is still mostly retained even after cycling. Such comparative SEM images for *m*Si-C electrodes before and after cycles further corroborate that the inner stress by volume change and consequently evolved cracking in electrodes can be effectively alleviated and buffered by unique structure of *m*Si-C composite, confirming its robust structural integrity over cycling [11,12,14,21].

With regard to practical application of Si as battery material, the packing density of materials plays a very important role and appreciably affects in determining the volumetric energy density of batteries [25,36]. It's well known that nano-sized electrode materials usually come with low volumetric capacities because of their low powder tap densities (<0.1 g/cm^3) [11,14,20]. Micro-sized particles, on the other hand, have relatively higher powder tap densities (>0.2 g/cm^3) due to few vacancies among constituting particles, contributing to higher volumetric capacities [11,14,20]. In this work, our semimicro-sized *m*Si-C composite has a high tap density (0.448 g/cm^3), over three times higher than that of commercial Si NPs (0.134 g/cm^3). As described in experimental section, the tap density of our composite was obtained by calculating the ratio of sample mass to its tapped volume [25]. Although the primary particle of our composite is commercial Si NPs, such an enhancement of tap density can be ascribed to the unique agglomerate structure by interconnection of Si NPs covered with carbon nanolayers and carbonized polymer [11,21]. The *m*Si-C composite exhibits an impressive volumetric capacity above

933 mAh/cm^3, over two times higher than that of traditional graphite anodes (429 mAh/cm^3) [14,21]. Considering the importance of high volumetric capacity in the practical battery application, we believe our *m*Si-C composite has a high potential to be employed as anode material for practical battery applications. It should note that lowering of volumetric capacity considering the increase of electrode thickness after lithiation would be inevitable. Considering that *m*Si-C possesses wide ranges of pores, however, the extent of decrease in volumetric capacity is expected to be moderate. Engineering of the electrode architectures considering the overall volume change and their corresponding volumetric capacity will be our next subject of research.

4. Conclusions

In summary, we present a facile and scalable fabrication of semimicro-size agglomerate structured Si-carbon composite (*m*Si-C) through an aerosol process and carbon layer deposition for the LIB anode application. As-formed *m*Si-C composite is composed of interconnected Si NPs coated with conductive carbon layer, where Si NPs are uniformly distributed throughout the composite as primary building units. In the electrochemical test, the *m*Si-C composite exhibited a high initial reversible capacity (2084 mAh/g), good cycling stability (81% retention, 1694 mAh/g at 0.4 A/g) and coulombic efficiency (98.8%) within 100 cycles. Such good electrochemical performance of the *m*Si-C composite can be mainly attributed to its unique structure which sustains electronic/ionic conductivity during continuous lithiation/delithiation by 1) significantly mitigating the stress from volume change of Si, 2) providing more electronic pathways, 3) shortening the ionic diffusion length and 4) facilitating the formation of stable SEI layer. As for its practical application, the *m*Si-C composite exhibit impressive volumetric capacity (933 mAh/cm^3) owing to its high tap density (0.448 g/cm^3) stemming from unique composite structure.

The current study demonstrates that our facile and scalable synthetic process (aerosol process and carbon coating) can be viable methods for commercial production of LIB anode materials based on *m*Si-C composite. Taking the excellent performance of *m*Si-C composites into account, we believe *m*Si-C composite could be considered as practical and commercially producible anode materials for next generation high-energy LIBs.

Acknowledgements

This work was supported by the Assistant Secretary for Energy Efficiency and Renewable Energy, Office of Vehicle Technologies of the U.S. Department of Energy under Contract no. DE-EE0006447 (D. Wang) and by Basic Science Research Program through the National Research Foundation of Korea (NRF) funded by the Ministry of Education (No. NRF-2014R1A1A2058760) (Y.S. Jung).

Appendix A. Supplementary data

Supplementary data related to this article can be found at http://dx.doi.org/10.1016/j.jpowsour.2016.09.096.

References

[1] [a] M.S. Whittingham, Chem. Rev. 104 (2004) 4271–4301;
[b] X. Lai, J.E. Halpert, D. Wang, Energy Environ. Sci. 5 (2012) 5604–5618.
[2] [a] M.R. Zamfir, H.T. Nguyen, E. Moyen, Y.H. Lee, D.J. Pribat, Mater. Chem. A 1 (2013) 9566–9586;
[b] W. Xu, S.S. Vegunta, J.C. Flake, J. Power Sources 196 (2011) 8583–8589;
[c] X.H. Liu, L.Q. Zhang, L. Zhong, Y. Liu, H. Zheng, J.W. Wang, J.-H. Cho, S.A. Dayeh, S.T. Picraux, J.P. Sullivan, S.X. Mao, Z.Z. Ye, J.Y. Huang, Nano Lett. 11 (2011) 2251–2258;
[d] H. Sohn, D. Kim, J. Lee, S. Yoon, RSC Adv. 6 (2016) 39484–43949.
[3] [a] M.-H. Park, M.G. Kim, J. Joo, K. Kim, J. Kim, S. Ahn, Y. Cui, J. Cho, Nano Lett. 9 (2009) 3844–3847;
[b] H. Wu, G. Chan, J.W. Choi, I. Ryu, Y. Yao, M.T. McDowell, S.W. Lee, A. Jackson, Y. Yang, L. Hu, Y. Cui, Nat. Nanotechnol. 7 (2012) 310–315;
[c] S. Choi, J.C. Lee, O. Park, M.-J. Chun, N.-S. Choi, S.J. Park, Mater. Chem. A 1 (2013) 10617–10621;
[d] T. Song, J. Xia, J.-H. Lee, D.H. Lee, M.-S. Kwon, J.-M. Choi, J. Wu, S.K. Doo, H. Chang, W.I. Park, D.S. Zang, H. Kim, Y. Huang, K.-C. Hwang, J.A. Rogers, U. Paik, Nano Lett. 10 (2010) 1710–1716;
[e] Z. Wen, G. Lu, S. Mao, H. Kim, S. Cui, K. Yu, X. Huang, P.T. Hurley, O. Mao, J. Chen, Electrochem. Commun. 29 (2013) 67–70.
[4] H. Wu, G. Zheng, N. Liu, T.J. Carney, Y. Yang, Y. Cui, Nano Lett. 12 (2012) 904–909.
[5] T. Song, H. Cheng, H. Choi, J.-H. Lee, H. Han, D.H. Lee, D.S. Yoo, M.-S. Kwon, J.-M. Choi, S.G. Doo, H. Chang, J. Xiao, Y. Huang, W.I. Park, Y.-C. Chung, H. Kim, J.A. Rogers, U. Paik, ACS Nano 6 (2011) 303–309.
[6] [a] S.C. Jung, J.W. Choi, Y.-K. Han, Nano Lett. 12 (2012) 5342–5347;
[b] M.T. McDowell, S.W. Lee, J.T. Harris, B.A. Korgel, C. Wang, W.D. Nix, Y. Cui, Nano Lett. 13 (2013) 758–764;
[c] J.W. Wang, Y. He, F. Fan, X.H. Liu, S. Xia, Y. Liu, C.T. Harris, H. Li, J.Y. Huang, S.X. Mao, T. Zhu, Nano Lett. 13 (2013) 709–715;
[d] S. Huang, T. Zhu, J. Power Sources 196 (2011) 3664–3668.
[7] [a] S.-H. Ng, J. Wang, D. Wexler, K. Konstantinov, Z.-P. Guo, H.-K. Liu, Angew. Chem. Int. Ed. 45 (2006) 6896–6899;
[b] L. Shen, Z. Wang, L. Chen, Carbon-coated hierarchically porous silicon as anode material for lithium ion batteries, RSC Adv. 4 (2014) 15314–15318.
[8] D.S. Jung, T.H. Hwang, S.B. Park, J.W. Choi, Nano Lett. 13 (2013) 2092–2097.
[9] [a] P.R. Abel, Y.-M. Lin, H. Celio, A. Heller, C.B. Mullins, ACS Nano 6 (2012) 2506–2516;
[b] Z. Lu, J. Zhu, D. Sim, W. Zhou, W. Shi, H.H. Hng, Q. Yan, Chem. Mater. 23 (2011) 5293–5295.
[10] M.K. Datta, J. Maranchi, S.J. Chung, R. Epur, K. Kadakia, P. Jampani, P.N. Kumta, Electrochim. Acta 56 (2011) 4717–4723.
[11] [a] X.H. Liu, L. Zhong, S. Huang, S.X. Mao, T. Zhu, J.Y. Huang, ACS Nano 6 (2012) 1522–1531;
[b] H. Kim, M. Seo, M.H. Park, J. Cho, Angew. Chem. Int. Ed. 49 (2010) 2146–2149.
[12] [a] B. Wang, X. Li, X. Zhang, B. Luo, Y. Zhang, L. Zhi, Adv. Mater. 25 (2013) 3560–3565;
[b] S. Chen, M.L. Gordin, R. Yi, G. Howlett, H. Sohn, D. Wang, Phys. Chem. Chem. Phys. 14 (2012) 12741–12745;
[c] Y. Park, N.-S. Choi, S. Park, S.H. Woo, S. Sim, B.Y. Jang, S.M. Oh, S. Park, J. Cho, K.T. Lee, Adv. Energy Mater. 3 (2013) 206–212.
[13] H.C. Tao, L.Z. Fan, X. Qu, Electrochim. Acta 71 (2012) 194–200.
[14] [a] R. Yi, F. Dai, M.L. Gordin, S. Chen, D. Wang, Adv. Energy Mater. 3 (2013) 295–300;
[b] R. Yi, F. Dai, M.L. Gordin, H. Sohn, D. Wang, Adv. Energy Mater. 3 (2013) 1507–1515.
[15] R. Huang, X. Fan, W. Shen, J. Zhu, Appl. Phys. Lett. 95 (2009) 133119–133121.
[16] M. Gu, Y. Li, X. Li, S. Hu, X. Zhang, W. Xu, S. Thevuthasan, D.R. Baer, J.-G. Zhang, J. Liu, C. Wang, ACS Nano 6 (2012) 8439–8447.
[17] A. Magasinski, P. Dixon, B. Hertzberg, A. Kvit, J. Ayala, G. Yushin, Nat. Mater. 9 (2010) 353–358.
[18] X. Zhou, Y.-X. Yin, L.-J. Wan, Y.-G. Guo, Chem. Commun. 48 (2012) 2198–2200.
[19] A. Gohier, B. Laik, K.-H. Kim, J.-L. Maurice, J.-P. Pereira-Ramos, C.S. Cojocaru, P.T. Van, Adv. Mater. 24 (2012) 2592–2597.
[20] [a] K. McCormac, I. Byrd, R. Brannen, B. Seymour, J. Li, J. Wu, Phys. Status Solidi A 212 (2015) 877–881;
[b] X. Liu, K. Xie, C.-M. Zeng, J. Wang, Z. Jing, J. Power Sources 214 (2012) 119–123;
[c] E. Park, H. Yoo, J. Lee, M.-S. Park, Y.-J. Kim, H. Kim, ACS Nano 9 (2015) 7690–7696;
[d] X. Wang, M. Xi, F. Zheng, B. Ding, H. Fong, Z. Zhu, Nano Energy 12 (2015) 794–800.
[21] [a] J. Song, S. Chen, M. Zhou, T. Xu, D. Lv, M.L. Gordin, T. Long, M. Melnyk, D. Wang, J. Mater. Chem. A 2 (2014) 1257–1262;
[b] J.R. Szczech, S. Jin, Energy Environ. Sci. 4 (2011) 56–72;
[c] H. Kim, B. Han, J. Choo, J. Cho, Angew. Chem. Int. Ed. 47 (2008) 10151–10154;
[d] J.I. Lee, K.T. Lee, J. Cho, J. Kim, N.S. Choi, S. Park, Angew. Chem. Int. Ed. 51 (2012) 2767–2771.
[22] D. Hristozov, I. Malsch, Sustainability 1 (2009) 1161–1194.
[23] N. Liu, Z. Lu, J. Zhao, M.T. McDowell, H.-W. Lee, W. Zhao, Y. Cui, Nat. Mater. 9 (2014) 187–192.
[24] [a] H. Sohn, Z. Chen, Y.S. Jung, Q. Xiao, M. Cai, H. Wang, Y. Lu, J. Mater. Chem. A 1 (2013) 4539–4545;
[b] Q. Xiao, H. Sohn, Z. Chen, D. Toso, M. Mechlenburg, Z.H. Zhou, E. Poirier, A. Dailly, H. Wang, Z. Wu, M. Cai, Y. Lu, Angew. Chem. Int. Ed. 51 (2012) 10546–10550.
[25] [a] T. Xu, J. Song, M.L. Gordin, H. Sohn, Z. Yu, S. Chen, D. Wang, ACS Appl. Mater. Interfaces 5 (2013) 11355–11362;
[b] H. Sohn, M.L. Gordin, M. Regula, D.H. Kim, Y.S. Jung, J. Song, D. Wang,

J. Power Sources 302 (2016) 70–78.
[26] A. Magasinski, B. Zdyrko, I. Kovalenko, B. Hertzberg, R. Burtovyy, C.F. Huebner, T.F. Fuller, I. Luzinov, G. Yushin, ACS Appl. Mater. Interfaces 2 (2010) 3004–3010.
[27] [a] S.M. Kang, K.M. Ahn, B.T. Ahn, J. Electrochem. Soc. 159 (2012) H29–H32;
[b] B. Li, D. Yu, S.-L. Zhang, Phys. Rev. B 59 (1999) 1645–1648;
[c] R. Wang, G. Zhou, Y. Liu, S. Pan, H. Zhang, D. Yu, Z. Zhang, Phys. Rev. B 61 (2000) 16827–16931;
[d] Y.-S. Hu, R. Demir-Cakan, M.-M. Titirici, J.-O. Muller, R. Schlogl, M. Antonietti, J. Maier, Angew. Chem. Int. Ed. 47 (2008) 1645–1649;
[e] B. Parida, J. Choi, G. Lim, K. Kim, K. Kim, J. Nanomater. 2013 (2013) 953790–953799.
[28] Y.S. Jung, K.T. Lee, S.M. Oh, Electrochim. Acta 52 (2007) 7061–7067.
[29] A. Kim, S. Lim, D.-H. Peck, S.-K. Kim, B. Lee, D. Jung, Nanomaterials 2 (2012) 206–216.
[30] T. Zheng, Y. Liu, E. Fuller, S. Tseng, U.V. Sacken, J. Dahn, J. Electrochem. Soc. 142 (1995) 2581–2590.
[31] Y.-M. Lin, K.C. Klavetter, P.R. Abel, N.C. Davy, J.L. Snider, A. Heller, C.B. Mullins, Chem. Commun. 48 (2012) 7268–7270.
[32] J. Guo, A. Sun, X. Chen, C. Wang, A. Manivannan, Electrochim. Acta 56 (2011) 3981–3987.
[33] J.Y. Eom, J.W. Park, H.S. Kwon, S. Rajendran, J. Electrochem. Soc. 153 (2006) A1678–A1684.
[34] [a] S. Laruelle, S. Grugeon, P. Poizot, M. Dolle, L. Dupont, J.-M. Tarascon, J. Electrochem. Soc. 149 (2002) A627–A634;
[b] R. Debryvere, S. Laruelle, S. Grugeon, P. Poizot, D. Gonbeau, J.-M. Tarascon, Chem. Mater. 16 (2004) 1056–1061;
[c] J. Jamnik, J. Maier, Phys. Chem. Chem. Phys. 5 (2003) 5215–5220;
[d] Y.F. Zhukovski, P. Balaya, E.A. Kotomin, J. Maier, Phys. Rev. Lett. 96 (2006) 058302.
[35] Y. Ren, A.R. Armstrong, F. Jiao, P.G. Bruce, J. Am. Chem. Soc. 132 (2010) 996–1004.
[36] J. Liu, Q. Zhang, Z.-Y. Wu, J.-T. Li, L. Huang, S.-G. Sun, ChemElectroChem 2 (2015) 611–616.